Check for updates

Ultrasensitive simultaneous detection of lead and cadmium in water using gold nanocluster-modified gold electrodes†

Shunyao Jia,[a] Yuanping Li, [ID] *[a] Yaoning Chen, [ID] *[b] Yanting Wu,[a] Tianyun Zhou,[a] Nianping Chi,[a] GuoWen He,*[c] Wei Zhang,[a] Wenqiang Luo,[a] Hao Li[a] and Yumei Deng[a]

Heavy metals (HMs) pose significant environmental risks due to their widespread presence. In particular, lead (Pb) and cadmium (Cd) can accumulate in the human body through prolonged exposure or bioaccumulation *via* the food chain, presenting substantial threats to human health and ecosystems. This study developed a novel electrochemical sensing platform for simultaneous detection of trace Pb^{2+} and Cd^{2+} using a bare gold electrode modified with gold nanoclusters (GNPs-Au) through a potentiostatic method. Through systematic optimization of deposition parameters including 2 mmol per L $HAuCl_4$, 0.2 V deposition potential, and 80 s deposition time, the modified electrode exhibited 7.2-fold increased surface area compared to the bare gold electrode, as confirmed by field emission scanning electron microscopy (FESEM) and electrochemical characterization. The enhanced surface area provided abundant electrochemical reaction sites, significantly improving detection sensitivity. Under optimal detection conditions comprising pH 3.3, −4 V enrichment potential, and 390 s enrichment time, the modified electrode demonstrated linear responses for Pb^{2+} and Cd^{2+} in the range of 1–250 μg L^{-1} with a detection limit of 1 ng L^{-1}. The spike-recovery test yielded quantitative recoveries ranging from 90.86% to 113.47%. The interference experiment confirmed Cu^{2+} has a significant effect on the measurement. Moreover, the method successfully detected Pb^{2+} and Cd^{2+} in real water samples, with results showing minor errors compared to atomic absorption spectroscopy (AAS). These findings demonstrate the robust potential of GNPs-Au for trace heavy metal ion detection in environmental monitoring.

1. Introduction

With the rapid development of urbanization, industrialization and agricultural production activities, the use of a variety of products containing HMs and the random discharge of industrial wastewater, waste gas, waste residue, *etc.*, has led to the entry of excessive HMs into the environment; many countries have strict regulations on the discharge of HMs.[1,2] While trace metals such as copper ions (Cu^{2+}) and iron ions (Fe^{2+}) are beneficial to human health, most HMs are present in trace form in the water. They can cause damage to human health and cannot be biodegraded.[3–5] The degree of hazard varies depending on the concentrations and chemical forms in which they are present.[6,7] In particular, Pb and Cd exist in various

[a]School of Municipal and Geomatics Engineering, Hunan City University, Yiyang, Hunan 413000, China. E-mail: yuanpingli@hncu.edu.cn

[b]College of Environmental Science and Engineering, Hunan University and Key Laboratory of Environmental Biology and Pollution Control (Hunan University), Ministry of Education, Changsha 410082, China. E-mail: cyn@hnu.edu.cn

[c]School of Materials and Chemical Engineering, Hunan City University, Yiyang, Hunan 413000, China. E-mail: zhongyihgw@163.com

† Electronic supplementary information (ESI) available. See DOI: https://doi.org/10.1039/d5ra02612a

forms (inorganic, organic or mixed) in the environment, and long-term exposure or bioaccumulation through the food chain into the human body can harm the brain, central nervous system, immune system, kidneys and other organs, resulting in a variety of acute and chronic diseases.[1,4,8] Rapidly and accurately measuring the concentration of HMs in the aqueous environments and their existence status is the primary task in the prevention and control of heavy metal pollution in water. However, in the aquatic environment, the coexistence of multiple heavy metal ions, the matrix of water and the compound pollution of organic matter-heavy metals have great negative impacts on the accuracy of routine detection and uncertainty for the selection of pollution management strategies. How to achieve the qualitative and quantitative detection of HMs in the aquatic environment accurately and effectively is an urgent problem for researchers to solve, which is of significant significance to ensure the accurate acquisition of heavy metal information.[9]

Traditional analytical methods for heavy metal detection include spectrophotometry, inductively coupled plasma mass spectrometry (ICP-MS), atomic absorption spectrometry (AAS), atomic fluorescence spectrometry (AFS), X-ray fluorescence spectrometry, *etc.*[10–13] However, most of the above methods have

large equipment, high operating costs, cumbersome and complex sample pretreatment processes, and most of them can only perform total amount detection, making it difficult to individually analyze specific HMs in complex samples, and real-time online detection is difficult to achieve. Therefore, the use of highly sensitive and specific sensing detection technology to analyze HMs has become a new research hotspot, and its equipment tends to be miniaturized and easy to operate, which can achieve rapid, efficient, real-time and online detection of trace HMs in the aquatic environment.

In recent years, sensing analysis techniques for heavy metals detection have significantly been developed, including electrochemical, fluorescence, colorimetric, photoelectrochemical, surface plasmon resonance, surface Raman spectral scattering, *etc.*[14–16] The use of specific functional materials includes fluorophores, oxidoreductase enzymes, conjugated polymers, embedding agents, quantum dot and nanomaterials, *etc.*[17–22] The use of these materials not only enriches the construction strategies for sensing analyses but also effectively improves the performance of the sensing and detection strategies due to the unique and excellent properties of each of them. In comparison, the colorimetric method is intuitive but not sensitive enough; the fluorescence technique has better sensitivity, but the fluorescent indicator is susceptible to interference, leading to false-positive results;[23] and although the development of quantum dots technology can effectively avoid the problem of false-positive results, further proof is needed to determine whether quantum dots are a safe indicator;[24] electrochemical methods are relatively simple and stable, and also show excellent detection sensitivity and flexibility in sensor construction and detection strategies.[2,25,26]

In electrochemical techniques, various materials can be employed for electrode modification. Metal–organic frameworks (MOFs), coordination networks formed by metal nodes bridged with organic linkers, demonstrate effectiveness in detecting Pb^{2+} and Cd^{2+} in aqueous systems.[27,28] Gajanan A. Bodkhe *et al.* developed a Au nanoparticle/single-walled carbon nanotube (SWNT) nanocomposite-incorporated copper benzene tricarboxylate framework (Au/SWNTs@MOF-199) for Pb^{2+} detection, achieving a linear range from 0.1 mM to 1 pM ($R^2 = 0.9958$) with a detection limit of 25 pM.[29] Zhao *et al.* fabricated ZIF-67-derived cobalt/nitrogen-doped carbon polyhedrons interconnected with multiwalled carbon nanotubes (termed Co@NC/MWCNT) for Cd^{2+} detection, demonstrating a linear response range of 0.12–2.50 μM with a correlation coefficient of 0.99 (R^2).[30] These studies confirm that MOF-based sensors achieve both sensitive individual detection of Pb^{2+} and Cd^{2+} and comparable analytical performance in their simultaneous quantification, demonstrating equivalent detection capabilities in single-ion and co-detection modes. The integration of zeolitic Imidazolate Framework-8 (ZIF-8) with bismuth complexes and carboxylated multi-walled carbon nanotubes on the glassy carbon electrode (GCE) effectively addresses the inherent conductivity limitations of conventional MOFs, achieving detection limits for Pb and Cd as low as 0.76 μg L^{-1} and 0.87 μg L^{-1}, respectively. This optimized sensor demonstrates superior performance in practical applications, enabling

reliable detection of both HMs in complex aqueous environments, including lake water and wastewater treatment plant effluent samples.[28] When Ag-doped MOF nanoparticles with a large specific surface area and conductive network were used to co-modify pure electrodes with chitosan (CHI), they not only improved charge transfer on the surface of the imprinted electrode but also modulated the accessibility and selectivity of the sensor electrode to the target. This enhancement increased detection capability and sensitivity, achieving a limit of detection for Pb and Cd in aqueous environments as low as 1.0×10^{-10} mol L^{-1}.[27,31] The GCE was modified with covalent organic frameworks (COFs) synthesized from graphene (GR), 2,5-dimethoxybenzaldehyde (DMTP), and 1,3,5-tris(4-aminophenyl) benzene (TAPB) *via* a deamidation condensation reaction. This modification enhanced the electrode's specific surface area, periodic porous network, and the number of effective binding sites, leading to improved electrical conductivity. Consequently, the sensor achieved detection limits for Pb and Cd of 8.747 nM and 0.011 μM, respectively.[32] In addition to the modification of conventional electrodes using MOFs and COFs, disposable graphite screen-printed electrodes (GSPEs) can be easily modified through the adsorption of metal ions by the non-toxic post-transition metal bismuth (Bi). The bismuth imidazolate-based sensor exhibits linear responses in two concentration ranges: 10–100 μg L^{-1} and 1–10 μg L^{-1}.[33] Moreover, a screen-printed carbon ink electrode modified with bismuth powder (Bi-SPE) was developed for Cd^{2+} detection, demonstrating a linear range of 5–50 μg L^{-1} and a detection limit of 4.80 μg L^{-1}.[34] Alternatively, gel electrolytes can be prepared by dissolving pectin in potassium chloride (KCl), mixed with an Sb(III)–Bi(III) antimony alloy solution, and casting onto a paper substrate. And an *in situ* doped bismuth nanoparticle-modified screen-printed graphene electrode can be used to prepare bismuth film electrodes.[35,36] Its application in the simultaneous detection of Pb and Cd is environmentally friendly, stable and exhibits high detection accuracy.[37,38] However, these composite electrodes are difficult to prepare, highlighting the need for an electrode that is not only easy to prepare but also highly sensitive for detection.

The application of novel nanofunctional materials as electrode modifications in the field of sensing and analysis is becoming more and more widespread, which is the current trend in the development of sensing and analysis technology. Among them, GNPs with superior electron conductivity and biomolecular adaptability have attracted much attention.[39] The spatial structure of GNPs can provide a huge contact reaction specific surface area and spatial sites.[40] It has been applied to construct biosensors such as immunosensors and enzymes, and has demonstrated good performance.[41] Therefore, Mohamad Nor *et al.*[42] enhanced the performance of indium tin oxide (ITO) electrodes by functionalizing them with 3-aminopropyltriethoxysilane (APTES) modifying with gold nanoparticles (AuNPs). This modification leveraged the excellent electrical conductivity, high electrocatalytic activity, and substantial surface area of AuNPs to improve the electrode's efficacy in detecting Pb^{2+} and Cd^{2+} simultaneously. Utilizing square-wave anodic stripping voltammetry (SWASV), the sensor

achieved detection limits of 0.90 ppb for Pb and 0.73 ppb for Cd in water. Additionally, Zhao et al.[43] developed a sensitive electrochemical sensor by modifying the GCE with a nanocomposite film comprising reduced graphene oxide (RGO) and gold nanoparticles (AuNPs), followed by a Nafion coating. This modification enhanced the electrode's surface area and conductivity, facilitating the simultaneous detection of Pb^{2+} and Cd^{2+} in soil samples. The sensor demonstrated a detection limit of 0.7 $\mu g\ L^{-1}$ for Cd^{2+} and 0.3 $\mu g\ L^{-1}$ for Pb^{2+}, indicating high sensitivity and selectivity for these HMs. Zhu et al.[44] developed a bismuth film-modified GCE by incorporating a nanocomposite of gold nanoparticles (AuNPs), graphene (GN), and cysteine (Cys) (Au–GN–Cys). This modification enhanced the electrode's surface area and electrical conductivity, facilitating the deposition of Pb^{2+} and Cd^{2+}. Under optimized conditions, the sensor achieved detection limits of0.05 $\mu g\ L^{-1}$ for Pb^{2+} and 0.10 $\mu g\ L^{-1}$ for Cd^{2+}. These studies indicate that gold nanoclusters (GNPs) have a positive role in enhancing sensitivity. However, it is rare to see modification of GNPs on the bare gold electrode for improving the detection sensitivity of the bare gold electrode. The bare gold electrode is mainly used to construct deoxyribonucleic acid (DNA), enzymes, biofuel cells and other biosensors.[45–47] Hence, it can achieve electrochemical detection of HMs with its advantages of cheapness, repeatable polishing and use, friendly interface, etc. However, the sensitivity of SWASV for the detection of trace HMs by directly using the bare gold electrode needs to be improved, and the modification of specific functional materials can reduce the detection limitation.[48] Therefore, attempts can be made to modify GNPs on the bare gold electrode to achieve good simultaneous trace detection of Pb^{2+} and Cd^{2+} in water.

GNPs have garnered growing interest in electrochemical sensing applications owing to their unique quantum size effects, which enhance specific surface area, increase accessible electrochemical active sites, improve electrode conductivity, and promote efficient electron transfer.[39,44] We propose that the functionalization of the bare gold electrode with GNPs enables the fabrication of innovative three-dimensional nanocomposite electrodes, thereby creating new possibilities for developing GNPs-Au with enhanced heavy metals' detection precision. This study presents a novel nanocomposite GNPs-Au utilizing SWASV for the simultaneous detection of trace Pb^{2+} and Cd^{2+}. Systematic optimization of electrochemical parameters was conducted to establish optimal analytical conditions. The GNPs-Au performance was rigorously validated through interference resistance assessment, standard recovery tests, and practical detection in environmental water matrices.

2. Materials and methods

2.1 Materials

Electrochemical measurements were conducted using a CHI 660E electrochemical workstation (Shanghai Zhenhua Instrument Co., China). Material characterization was performed on an MIRA3 field emission scanning electron microscope (TESCAN, Czech Republic). Elemental analysis was carried out using an AA-7000 atomic absorption spectrophotometer (Beijing

Pgeneral Analytical Instrument Co., China). A conventional three-electrode system comprising a 2.0 mm Au working electrode (Shanghai Zhenhua), Pt wire counter electrode (Shanghai Zhenhua), and Ag/AgCl reference electrode (3 M KCl filling solution) was employed.

The Piranha solution was prepared by mixing 98% concentrated sulfuric acid and 30% hydrogen peroxide at a volume ratio of 3 : 1. The experimental solutions included: 10 mmol per L $HAuCl_4$; 5 mmol per L $K_3Fe(CN)_6$; 100 mmol per L KCl; 0.5 mol per L H_2SO_4; 100 mg per L $CuSO_4$; 100 mg per L $MnCl_2$; 100 mg per L $CrCl_3$; 100 mg per L zinc acetate ($Zn(CH_3COO)_2$); 4.83 × 10^{-4} mol per L $Pb(NO_3)_2$; 8.93 × 10^{-4} mol per L $CdCl_2$; a series of ABS with pH of 2.3, 2.5, 2.7, 2.9, 3.3, 3.5, 3.9, 4.4, and 4.9 were prepared by mixing acetic acid (CH_3COOH) and potassium acetate (CH_3COOK) in varying mass ratios. All solutions were prepared using deionized water and analytical-grade reagents.

2.2 Modification and characterization of gold nanoclusters

The bare gold electrode (d = 2.0 mm) was polished with 0.3 and 0.05 μm alumina powder from the coarse particle size to the fine particle size. Then, it was polished in one direction on 2500, 3000, 5000, and 7000 mesh metallographic sandpaper. Finally, it was polished on the polishing cloth of polymer synthetic leather. The polished electrode was placed into the Piranha solution and soaked for 3 h. It was immersed in acetone for 10 minutes and underwent ultrasonic cleaning in acetone for 10 seconds to remove the possible organic impurities on the surface. The cleaned electrode was placed in 0.5 mol per L H_2SO_4. Cyclic voltammetry (CV) scanning (scanning rate of 100 mV s^{-1}) was conducted in the range of −0.4 V to 1.0 V. The electrochemical treatment was repeated until the detected current was stable. After electrochemical treatment, the surface electrochemical characteristics of the bare gold electrode were characterized via CV scanning with potassium ferricyanide solution (5 × 10^{-3} mol per L $K_3Fe(CN)_6$ + 0.1 mol per L KCl) as the bottom solution to facilitate the subsequent steps of GNPs modification, heavy metal enrichment, and heavy metal stripping. The results can be compared with the change in electrochemical characteristics of the bare gold electrode surface.

The different concentration gradients of $HAuCl_4$ (0.005, 0.01, 0.05, 0.1, 0.5, 1, 1.5, 2, and 2.5 mmol L^{-1}) were used to modify the activated gold electrode via the potentiostatic method. The electrochemical properties of each concentration gradient were characterized by CV at different deposition potentials (−0.5, −0.3, −0.1, 0.1, 0.3, and 0.5 V). The peak current of each time was extracted to draw a dual-parameter optimization plot, which was analyzed to obtain the optimal deposition concentration and potential. The peak currents of cyclic voltammograms at different deposition times (20, 40, 60, 80, and 100 s) was extracted to optimize the deposition time of GNPs at the optimal deposition concentration and potential. Each step was characterized using FESEM and CV.

2.3 Parameter optimization of modified electrode

The use of SWASV for qualitative and quantitative detection of HMs is the key parameter in pH of the ABS and the enrichment

of potential and time. The electrochemical detection of GNP-Au can be considerably influenced. Therefore, pH of the ABS, the enrichment of the potential and time must be optimized before the quantitative analysis of heavy metal ions to allow GNPs-Au to obtain a high current response, sensitivity, and wide detection range. Moreover, the excellent performance of GNPs-Au electrochemical detection can be ensured.

The effect of solution pH on current response was systematically investigated under controlled electrochemical conditions: a deposition potential of -0.6 V ($vs.$ Ag/AgCl), 100 s enrichment time, and 50 µg per L Pb^{2+} and Cd^{2+} standard solution in 0.2 mol per L ABS with pH adjusted to 2.3, 2.5, 2.7, 2.9, 3.3, 3.5, 3.9, 4.4, and 4.9.

Under optimized conditions including 0.2 mol per L ABS, pH 3.3, 200 s enrichment time, and 100 µg per L Pb^{2+} and Cd^{2+} concentrations, the optimal deposition potential was determined by measuring elution peak currents across six test potentials: -5, -4, -3, -2, -1, and $+1$ V.

Using 0.2 mol per L ABS containing 100 µg per L Pb^{2+} and Cd^{2+} at pH 3.3 with a deposition potential of -4 V, the optimal enrichment time was determined by analyzing stripping peak current through chronoamperometric measurements.

2.4 Qualitative and quantitative detection of heavy metals

Calibration standards containing Pb^{2+} and Cd^{2+} (1, 5, 10, 50, 110, 150, 210, 250 µg L^{-1}) in 0.2 mol per L ABS (pH = 3.3) were analyzed by standard addition method. All measurements maintained -4 V deposition potential with 390 s enrichment time while recording stripping peak current across the concentration series. In the electrochemical workstation, SWASV was used to enrich and dissolve the solution. The SWASV curves under different metal ion concentrations were obtained, and the stripping peak potentials and currents of Pb^{2+} and Cd^{2+} were recorded. Finally, the linear regression equation was drawn according to the relationship between peak current and concentration. Moreover, the mechanism is shown in Fig. 1.

2.5 Recovery experiment

According to the linear detection range of Pb^{2+} and Cd^{2+}, the concentration gradients of 4, 8, 40, 100, and 200 µg per L Pb^{2+}
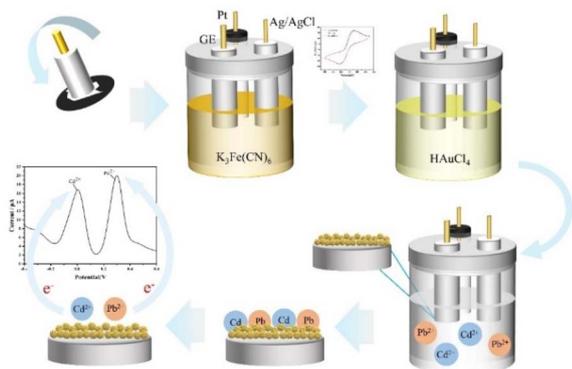

Fig. 1 Detection procedure of Pb^{2+} and Cd^{2+} via GNPs-Au.

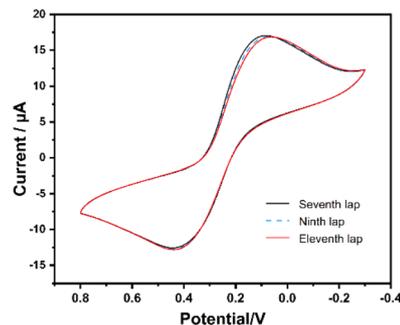**Fig. 2** Cyclic voltammogram of the bare gold electrode (in solution of 0.5 mol per L H_2SO_4; $vs.$ Ag/AgCl reference electrode).

and Cd^{2+} solutions were prepared for the recovery experiment. All electrochemical measurements were strictly conducted in 0.2 mol per L ABS (pH = 3.3) with controlled parameters: -4 V enrichment potential and 390 s enrichment time.

2.6 Interference experiment

In 0.2 mol per L ABS (pH = 3.3), the enrichment potential was -4 V, and the enrichment time was 390 s. The effects of other heavy metal ions on the Pb^{2+} and Cd^{2+} stripping peaks were investigated. In solutions with Pb^{2+} and Cd^{2+} concentrations of 40 µg L^{-1}, 40 µg L^{-1} of Zn^{2+}, Cr^{3+}, Mn^{2+} and Cu^{2+} were added to study the changes in the peak potentials and peak currents of Pb^{2+} and Cd^{2+}. Then, solutions with a concentration gradient of 4, 40, and 160 µg L^{-1} were prepared using Cu^{2+}, the metal ion with the greatest interference. It was agreed to keep the Pb^{2+} and Cd^{2+} concentrations at 40 µg L^{-1}. This method is intended to study the effect of increasing the concentration of Cu^{2+}, the metal ion with the greatest interference, on the stripping peaks of Pb^{2+} and Cd^{2+}.

2.7 Real water sample collection and spectrophotometric measurement

Water samples were collected from 4 sampling sites in Xiang River Basin, China. Table S1† shows the sampling locations and the measured pH.

Four samples of the real water were pretreated via the suction filtration method. Assemble the filter extraction device and place the filter membrane in a Brinell funnel with appropriate trimming. The filter paper was moistened with drops of distilled water so that the filter paper was tightly attached to the Brinell funnel. The pump was switched on, and four water samples were filtered one by one. The filtered water samples were stored in volumetric flasks for subsequent testing.

The standard solutions of Pb^{2+} and Cd^{2+} at the concentrations of 1, 5, 10, 50, 110, 150, 210, and 250 µg L^{-1} were prepared using ultrapure water and ABS (pH = 3.3), respectively. Under the working conditions (Table S2†), the absorbance values of the standard solutions in ultrapure water were measured, and the calibration curves were drawn to analyze Pb^{2+} and Cd^{2+} in real water samples. The absorbance values of the standard solutions in ABS (pH = 3.3) were measured, and the calibration curves were drawn to analyze the standard addition (100 µg L^{-1})

of Pb^{2+} and Cd^{2+} in real water samples (adjust the pH at 3.3). The recovery was also calculated.

3. Results and discussions

3.1 Activation of gold electrode

The cleaned gold electrode was placed in 0.5 mol per L H_2SO_4 for CV scanning. The scanning potentials range was 0.3–0.8 V, and the scanning rate was 100 mV s^{-1}. The scanning curve with high repeatability was obtained by repeated scanning. The detection current was stabilized by repeated electrochemical treatment to remove the oxide layer on the electrode surface and expose the active sites on the electrode surface. As shown in Fig. 2, the CV curve has good repeatability, and an obvious oxidation peak and reduction peak of gold can be observed. The high coincidence degrees of the CV curves at the 7th, 9th, and 11th turns indicated that the oxide layer on the electrode surface was completely removed. The bare gold electrode can be used for further experiments.

3.2 Optimization of gold nanoclusters modified on the bare gold electrode

3.2.1 Gold nanoclusters modification concentration and deposition potential. Potentiostatic method was used to characterize the effect of different concentrations of $HAuCl_4$ on the bare gold electrode surface modification by electrodeposition. The GNPs deposition potential was optimized under different concentration gradients. Fig. 3 shows the changes of peak currents under different concentrations and potentials. The current value obtained the maximum when the $HAuCl_4$ was 2×10^{-3} mol L^{-1}, and the potential was 0.2 V. The current response value gradually increased with the increase of $HAuCl_4$ concentration, indicating that the GNPs deposited on the surface of the bare gold electrode gradually increased. The response signal tended to be saturated when the concentration of $HAuCl_4$ reached 2×10^{-3} mol L^{-1}. Thus, 2×10^{-3} mol per L $HAuCl_4$ was chosen as the optimal GNPs modification concentration. The current response value and the peak current value tended to decrease when the deposition potential was 0.2 V. According to
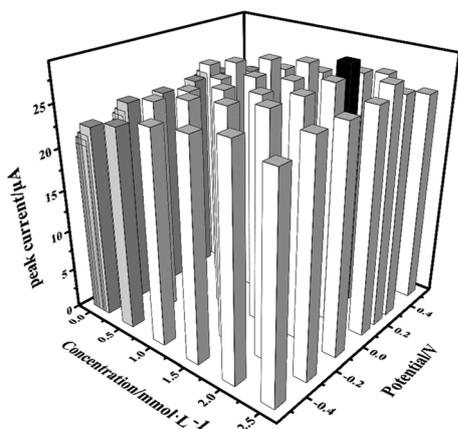
classical electrodeposition theories (the Butler–Volmer equation and the diffusion control model, e.g.), the maximization of the peak current relies on balancing the thermodynamic driving force with the kinetic limitations, and the optimal deposition voltage is a manifestation of this balance, whereas deviations from this voltage lead to a decrease in the current either by reducing the amount of effective deposition, introducing side reactions, or lowering the efficiency of the electron transfer.[49–52] Fig. 3 shows that there is the highest peak current at the optimal deposition voltage of 0.2 V, exhibiting the best electron transfer, indicating that the GNPs reach the maximum coverage and the best electron transfer efficiency on the electrode surface. If deviating from this voltage, the peak current decreases. Thus, 0.2 V was chosen as the optimal gold nanoclusters deposition potential.

3.2.2 Surface morphology analysis of the modified electrode. FESEM was used to analyze the surface morphology of GNPs-Au. FESEM images showed that, unlike the traditional plane structure electrode, a steric structure was formed on the micro interface of the bare gold electrode surface after GNPs deposition. GNPs were arranged on the bare gold electrode surface to form a base layer. A layer of GNPs was deposited, thereby providing a growth basis for GNPs formation in subsequent experiments and facilitating the stable formation of GNPs on the electrode surface. Its nonplanar structure could provide sufficient reaction sites and reaction space for the enrichment and stripping of HMs. This scenario was conducive to the entry of heavy metal ions into the reaction area. It also increased the site reactivity and the probability that the pre-concentration and stripping electrochemical signals were captured.[53] In theory, these factors improve the detection sensitivity of GNPs-Au. The observation was consistent with the conclusion that the peak current value of the CV curve increased by 131% after the GNPs were modified.

As shown in Fig. 4a, at an $HAuCl_4$ concentration of 0.5 mmol L^{-1}, GNPs exhibit an average diameter of approximately 10 nm, with a 60% surface coverage on the bare gold electrode (Fig. 4a). When the concentration of $HAuCl_4$ was 1 mmol L^{-1}, the average diameter of GNPs was approximately 15–20 nm, with a 70% surface coverage on the bare gold electrode (Fig. 4b). The average diameter of GNPs was approximately 30 nm, with a 90%
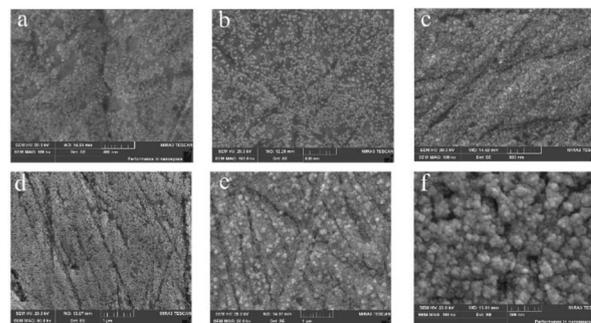

Fig. 3 Dual-parameter optimization of $HAuCl_4$ concentrations and deposition potentials.

Fig. 4 FESEM images of GNPs-Au surface formed by different concentrations of $HAuCl_4$ ((a) 0.5 mmol L^{-1}, (b) 1 mmol L^{-1}, (c) 2 mmol L^{-1}, (d) 4 mmol L^{-1}, (e) 7 mmol L^{-1}, (f) 10 mmol L^{-1}).

surface coverage on the bare gold electrode when the concentration of $HAuCl_4$ was 2×10^{-3} mol L^{-1} (Fig. 4c). When the concentration of $HAuCl_4$ was 4×10^{-3} mol L^{-1}, the average diameter of GNPs was approximately 50 nm, with a 90% surface coverage on the bare gold electrode, and an obvious sense of particle existed (Fig. 4d). The average diameter of GNPs was approximately 100 nm, with a 95% surface coverage on the bare gold electrode when the concentration of $HAuCl_4$ was 7×10^{-3} mol L^{-1} (Fig. 4e). When the concentration of $HAuCl_4$ was 1×10^{-2} mol L^{-1}, the average diameter of GNPs was approximately 150 nm, the steric structure was obvious like a polyhedron with large particles and thickness, and the surface coverage on the bare gold electrode was more than 95% (Fig. 4f). The average diameter of GNPs on the surface of the bare gold electrode was directly proportional to the $HAuCl_4$ concentrations, and GNPs formation was very stable. GNPs with a small average diameter could provide a large specific surface area of contact reaction, reaction activity sites, and reaction space. This characteristic was conducive to sensor quantum size effects improvement.[54] In the trade-off between particle size and spatial site resistance, the optimized strategy of 30 nm GNPs and moderate modification density was chosen, which can maximize the active sites and minimize diffusion limitation, and avoid the nanoclusters as well as the impediment of mass transfer caused by the over-dense modification.[40,41,43,55]

GNPs deposited on the bare gold electrode surface could considerably improve the specific surface area of the sensing electrode and increase the reaction site because of their steric structure when the $HAuCl_4$ concentration was the optimal modification gradient of 2×10^{-3} mol L^{-1} (Fig. 4c). The average diameter of gold nanoclusters was 30 nm. In theory, a bare gold electrode with a diameter of 2 mm can hold approximately 4.44×10^9 GNPs. Assuming that 90% of the surface area of the bare gold electrode was covered with gold nanoclusters and the length of gold nanoclusters was 60 nm. The calculation indicated that, in this case, the specific surface area of the electrode surface increased by 7.2 times after the GNPs were modified.

A high $HAuCl_4$ concentration (1×10^{-2} mol L^{-1}) formed large GNPs (Fig. 4f). The steric structure was obvious. The $HAuCl_4$ concentration was 5 times the optimal concentration of 2×10^{-3} mol L^{-1}. However, the electrochemical response signal was only increased by 7%. Therefore, the surface morphology of GNPs was not the main factor in determining the electrochemical signal. Instead, the key was the coverage of GNPs on the electrode surface and the increase of specific surface area caused by particle size. The results of the electrochemistry signal and FESEM images, when the $HAuCl_4$ concentration was 2×10^{-3} mol L^{-1}, showed that the specific surface area of GNPs was increased by 7.2 times, which met the need for a greatly enhanced electrical signal transmission. The further increase of $HAuCl_4$ concentration slowed down the growth rate of GNPs coverage on the electrode surface, increased the particle size, and made the surface morphology increasingly steric. However, the increase of electrical signal slowed down.[55] Thus, the excessively dense structure might hinder the stripping of Pb^{2+} and Cd^{2+}. Therefore, the $HAuCl_4$ concentration of 2×10^{-3} mol L^{-1} was taken as the optimal modification
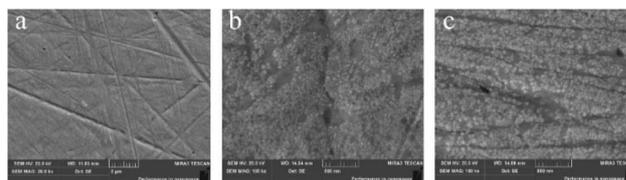

Fig. 5 (a) FESEM image of the bare gold electrode (b) FESEM image of the bare gold electrode was modified with gold nanoclusters with 0.5 mmol per L $HAuCl_4$ (c) FESEM image of GNPs–Au enrichment of Pb and Cd with 0.5 mmol per L $HAuCl_4$.

concentration, which had high comprehensive cost performance. At this time, GNPs-Au had a highly sensitive electrochemical response, which was consistent with the above conclusion.

The FESEM image of the bare gold electrode from the deposition of GNPs with a $HAuCl_4$ concentration of 5×10^{-4} mol L^{-1} to further enrich Pb and Cd is shown in Fig. 5. The FESEM image of the bare gold electrode was shown in Fig. 5a. When Pb and Cd were not enriched, GNPs were evenly distributed on the surface of the bare gold electrode (Fig. 5b), like four corners of a quadrilateral. GNPs dispersed in the four corners were pulled to the center to form agglomerates when Pb and Cd fell into it. Pb and Cd grow on the surface of GNPs and form branches like dendritic growths. Following Pb and Cd enrichment, agglomerates formed on the electrode surface (Fig. 5c). Two mechanisms were speculated to exist. One is a mechanism like that shown in Fig. 5b. The other mechanism was that the GNPs surface grew Pb and Cd, which looked like branches and leaves. The length of the branch could easily pull the surrounding GNPs, forming agglomerates. The morphology of Pb and Cd had no obvious difference because the sizes of Pb, Cd, and GNPs were very small. The steric structure had no obvious difference when the magnification was 100 000 times.

The high $HAuCl_4$ concentration of 1×10^{-2} mol L^{-1} was selected to observe the changes in the surface morphology of GNPs with the advancement of electrochemical detection steps. As shown in Fig. 6a, GNPs were enriched on the bare gold electrode surface, with an average diameter of 150 nm, high coverage, and uniform distribution of particles. As shown in Fig. 6b, the bare gold electrode surface of GNPs-Au enriched with Pb and Cd had a more steric particle structure than GNPs-Au, and the agglomeration phenomenon became obvious. The exposed part of the bare gold surface had fine particle distribution because of agglomeration. This observation was similar
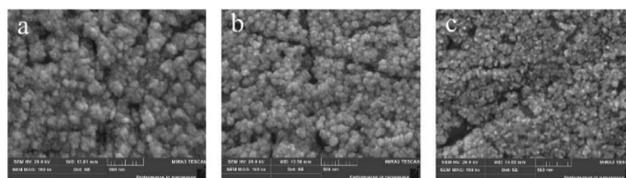

Fig. 6 (a) FESEM image of the bare gold electrode modified with 10 mmol per L $HAuCl_4$ (b) FESEM image of enrichment of Pb and Cd on the modified electrode (c) FESEM image of Pb^{2+} and Cd^{2+} stripping from the modified electrode.

to the FESEM images of copper plating. The subsequent interference experiments showed that Cu^{2+} had obvious interference with the stripping detection of Pb^{2+} and Cd^{2+}.[56] It also overlapped with the stripping peak of Pb^{2+} and made the stripping peak of Cd^{2+} drift away. Cu^{2+} was speculated to form alloy easily on the gold nanoclusters surface. This assumption was consistent with the conclusion that Cu^{2+} had interference in the Pb^{2+} and Cd^{2+} detection. As shown in Fig. 6c, the FESEM images of stripping after GNPs-Au enriched with Pb and Cd show that GNPs are like polyhedrons, the particles are agglomerated, and the coverage rate changes slightly. Compared with Fig. 6b and c shows no noticeable change in the surface morphology. This observation indicated that the GNPs were stable in structure, which was consistent with the conclusion that the GNPs-Au sensing electrode was kept at room temperature and used for electrochemical detection many times within 3 days. However, the response signal had no apparent attenuation.

The flatness of the bare gold electrode base was relatively poor. Enriching the GNPs in the gully was complicated. GNPs modification might also weaken the enrichment and stripping of heavy metal ions in the basement gullies, leading to signal instability. In the future, the polishing machine can be used to polish the electrode to improve the flatness of the base.

3.2.3 GNP deposition time. After the electrode was activated in 0.5 mol per L H_2SO_4, GNPs were electrodeposited in 2×10^{-3} mol per L $HAuCl_4$ at 0.2 V *via* potentiostatic method. The deposition time from 20 s to 100 s was investigated. After the modification, CV was performed in 5×10^{-3} mol per L $K_3Fe(CN)_6$ and 0.1 mol per L KCl solution. The test curve is shown in Fig. 7. The increase of deposition time increased the peak current. The increased current may be due to the start of proton reduction at the negative potential where the scanning begins, indicating that GNPs deposition had different degrees.[57] The longer the deposition time was, the more GNPs were deposited and the larger the surface area of the bare gold electrode was. The peak current of reduction increased obviously with the increase of deposition time. After 80 s, the peak
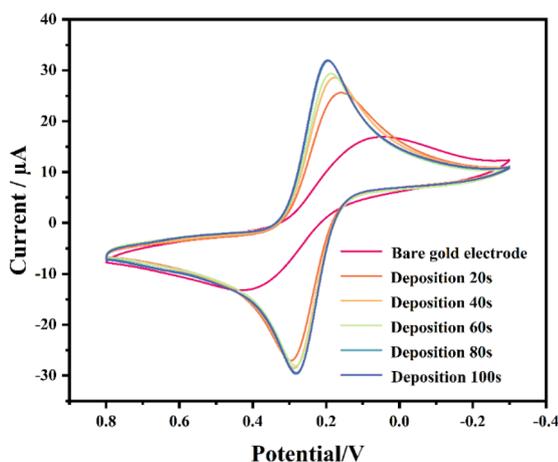
current tended to be saturated. Compared with the peak current of the bare gold electrode, the peak current of the bare gold electrode increased by 131% after 80 s. According to the fact that the essence of current saturation is the mechanism of combining mass transfer limitation (diffusion control) and surface position depletion, it is necessary to optimize the deposition time to avoid invalid deposition.[58–61] The optimal deposition time of GNPs was 80 s.

3.3 Optimization of the modified electrode to enrich Pb^{2+} and Cd^{2+}

3.3.1 pH. Optimizing the pH of the electrochemical detection solution is beneficial in maintaining the stability of GNPs-Au to capture the perfect response signal. In the case where both Pb^{2+} and Cd^{2+} exist in the reaction substrate, the response currents of Pb^{2+} and Cd^{2+} under different acidic conditions varies with pH, as shown in Fig. 8. Moreover, the peak current of Pb^{2+} reaches the maximum when pH is 2.3 at the time of simultaneous stripping. Then, the response current of Pb^{2+} drops when pH increases. Fig. 8 also shows that the response current of Cd^{2+} increases when the pH increases. The growth rate starts to slow down when the pH is 4.7. The possible reason based on analysis is that the high H^+ concentration based on low pH causes a reduction reaction on GNPs-Au surface, which competes with Cd^{2+}. This high H^+ concentration affects the Cd^{2+} deposition on the electrode surface, resulting in a low cadmium stripping peak current value. Despite the competition between H^+ and Cd^+ at low pH, Cd^+ can still be preferentially deposited at moderately negative potentials.[5,43,62,63] The OH^- near the electrode surface may easily undergo a complexation reaction with Pb^{2+} with the increase of pH, thereby affecting the Pb^{2+} deposition on the electrode surface.[4,64–66] When the pH is higher than 4, the metal ions are hydrolyzed, resulting in a reduced current signal.[63] This scenario leads to a drop in the Pb^{2+} stripping peak current. With every factor considered thoroughly, the interference of H^+ and OH^- on the electrode surface is relatively slight when pH reaches 3.3, and the stripping peak
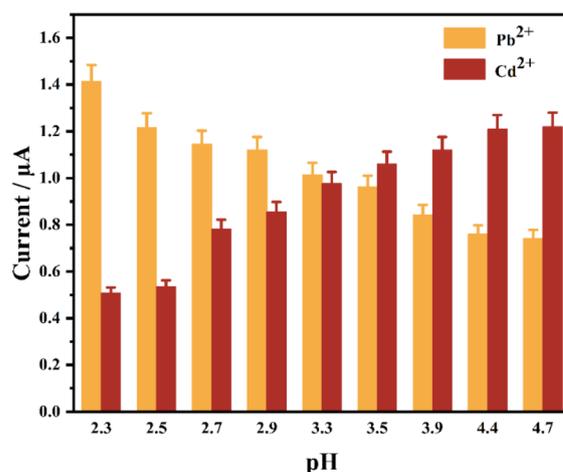

Fig. 7 Cyclic voltammograms of gold nanoclusters deposited on bare gold electrode for different deposition times (*vs.* Ag/AgCl reference electrode).

Fig. 8 Variation of Pb^{2+} and Cd^{2+} peak currents as different pH (*vs.* Ag/AgCl reference electrode).

currents of Pb^{2+} and Cd^{2+} are both considerable. Thus, the optimal performance of the reaction substrate solution and the stability of the electrochemical detective system are well guaranteed. Therefore, the optimal pH for simultaneous stripping detection is 3.3.

3.3.2 Enrichment potential. During the electrochemical conversion process, enriched heavy metal ions such as Pb^{2+} and Cd^{2+} undergo sequential reduction to their metallic states, followed by re-oxidation to ionic states. This redox cycling generates distinct current peaks. The peak potential corresponding to the peak current is the characteristic peak potential.[67] As shown in Fig. 9, a stripping peak appeared near +0.32 V when 50 μg per L Pb^{2+} was detected by SWASV. After adding 40 μg per L Cd^{2+} continually, a remarkable new stripping peak appeared near −0.05 V. Therefore, the stripping peak of Pb^{2+} was preliminarily determined to be approximately +0.32 V, whereas the stripping peak of Cd^{2+} was approximately −0.05 V. The former was in the positive pressure direction of the latter. According to the comparison between the redox potential of the elements and the stripping peak curve, the stripping peak of Pb^{2+} was near +0.35 V, and that of Cd^{2+} was near −0.05 V. Moreover, the peak potentials of Pb^{2+} and Cd^{2+} were quite different, and the two ions could be measured simultaneously.

The enrichment potential was optimized in 0.2 mol per L ABS (pH = 3.3), which contained 100 μg per L Pb^{2+} and 100 μg per L Cd^{2+}. The enrichment potentials ranged from −5 V to 1 V. The SWASV curves at different enrichment potentials are shown in Fig. 10. When the enrichment potentials were −1, −2, −3, −4
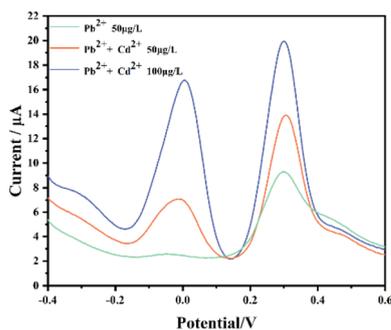
and −5 V, an abnormal interference peak could be observed near the stripping peak potential, which was +0.45 V. The position of the interference peak overlapped with the stripping peak of the Pb^{2+}. Thus, the stripping peak current of the Pb^{2+} would be considerably affected, and the quantitative analysis of Pb^{2+} would be interfered with. The possible reason for this interference peak was that the substances in the solution were oxidized to some intermediates at a positive potential, and the interference peak was formed by a reduction near +0.45 V during the forward scanning. The interference peak disappeared when the enrichment potential increased to −4 V. When the potential is too low, it tends to reduce other ions on the electrode, especially H^+, which will impair the deposition efficiency.[68] At this point, two evident stripping peaks could be observed. The peak currents of Pb^{2+} and Cd^{2+} on the stripping voltammetry curve were measured. In general, the stripping peak currents of Pb^{2+} and Cd^{2+} increased with the increase of the enrichment potential, and the different enrichment potentials affected the reduction rates of Pb^{2+} and Cd^{2+} during the enrichment process, thereby affecting the total amount of HMs that eventually accumulated on the surface of GNPs-Au. This scenario results in the change of the stripping peak current during the stripping process. The maximum stripping peak current of Cd^{2+} appeared when the enrichment potential was −3 V. However, an interference peak existed at +0.45 V. The stripping peak current of Cd^{2+} decreased sharply with the increase of the enrichment potential to −4 and −5 V. However, the stripping peak current of Pb^{2+} continued to increase slowly. Thus, −4 V was adopted as the optimal enrichment potentials to ensure that the peak currents of Pb^{2+} and Cd^{2+} reached the optimal value simultaneously. Under this enrichment potential, the peak currents of Pb^{2+} and Cd^{2+} were both large, and they did not have an interference peak, which was conducive to the subsequent electrochemical detection.

3.3.3 Enrichment time. The enrichment time was optimized in 0.2 mol per L ABS (pH = 3.3) containing 100 μg per L Pb^{2+} and 100 μg per L Cd^{2+}. The optimization range of enrichment time was 30 seconds to 420 seconds. The enrichment potential was set to −4 V. The SWASV curves under different enrichment time conditions are shown in Fig. 11. The stripping peaks of Pb^{2+} and Cd^{2+} could be observed in the SWASV curves, and no interference peak existed near the stripping peak. The

Fig. 9 Stripping voltammogram of Pb^{2+} and Cd^{2+} at varying concentrations in aqueous solutions (*vs.* Ag/AgCl reference electrode).

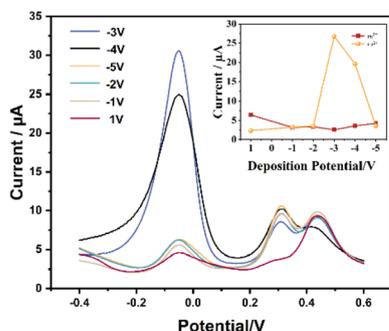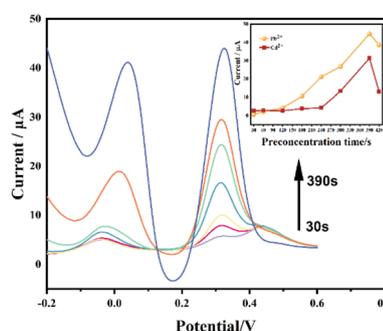**Fig. 10** Effect of enrichment potentials on stripping peaks of Pb^{2+} and Cd^{2+} in aqueous solutions (*vs.* Ag/AgCl reference electrode).

Fig. 11 Optimization of enrichment time for Pb^{2+} and Cd^{2+} detection *via* SWASV (*vs.* Ag/AgCl reference electrode).

Paper

stripping peak current increased with the enrichment time when the enrichment time was from 30 seconds to 390 seconds. The stripping peak currents of Pb^{2+} and Cd^{2+} in the SWASV curves could be extracted, and the enrichment time–peak current curves were drawn, as shown in Fig. 11. The stripping peak currents of Pb^{2+} and Cd^{2+} increased linearly when the enrichment time was from 30 seconds to 390 seconds. However, the stripping peak currents of Pb^{2+} and Cd^{2+} obviously decreased in sensitivity when the enrichment time increased from 390 s to 420 s. Moreover, the current intensity decreased with the increase of time. The reason might be that the electrode was saturated when the enrichment time was too long, affecting the detection of stripping peak current.[69,70] The decrease in current signal observed after 390 s was attributed to limited adsorption, reduced electron transfer, and electrode saturation, which limits adsorption and detection and may lead to desorption. The available active sites at the electrode interface were saturated.[55] Therefore, the enrichment time of 390 s was selected for subsequent electrochemical analysis with the consideration of the time consumption of voltammetric detection, sensitivity change, detection range, working electrode saturation, and other factors.

3.4 Application of the modified electrode in qualitative and quantitative detection of heavy metals

Quantitative analysis of Pb^{2+} and Cd^{2+} in 0.2 mol per L ABS at pH = 3.3 was conducted using optimized parameters with −4 V enrichment potential and 390 s enrichment time in combination with the standard addition method. Pb^{2+} and Cd^{2+} standard solution was added to ABS gradually, and the range from low concentration to high concentration was investigated. Different SWASV curves were obtained with the change in heavy metal concentrations. Moreover, the peak current of Pb^{2+} and

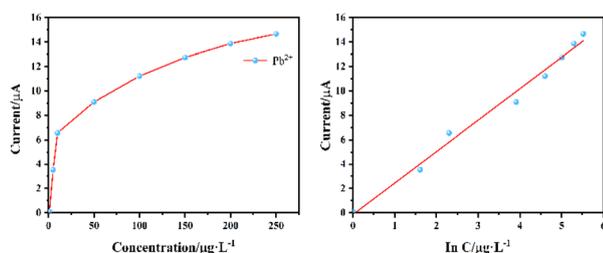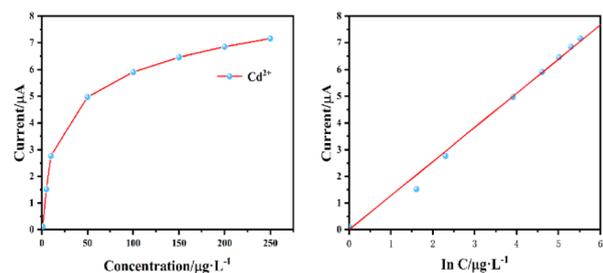**Fig. 12** Linear regression curve of Pb^{2+}.

Fig. 13 Linear regression curve of Cd^{2+}.

Table 1 Electrochemical detection of Pb^{2+} and Cd^{2+} standard recovery (buffer solution)

Elements	Concentrations	Measured concentrations	Tested sample 1	Tested sample 2	Tested sample 3	Average measured concentrations	Standard deviation	Coefficients of variation	Recovery
Pb^{2+}	4	7.847	8.421	8.036	8.86	8.439	0.412	4.89%	107.54%
	8	8.990	9.006	9.475	8.612	9.031	0.432	4.78%	100.45%
	40	11.644	9.589	10.343	11.808	10.58	1.128	10.66%	90.86%
	100	13.155	11.249	12.253	13.266	12.256	1.008	8.23%	93.16%
	200	14.298	12.375	13.923	13.137	13.145	0.774	5.89%	91.93%
Cd^{2+}	4	1.523	1.522	2.012	1.65	1.728	0.254	14.71%	113.47%
	8	2.468	3.028	2.653	2.677	2.786	0.210	7.53%	112.86%
	40	4.664	4.406	4.746	4.135	4.429	0.306	6.91%	94.96%
	100	5.914	5.788	6.175	7.171	6.378	0.713	11.19%	107.84%
	200	6.860	7.215	6.196	8.222	7.211	1.013	14.05%	105.12%

Cd^{2+} increased with the increase in heavy metal concentration. The stripping peak currents of Pb^{2+} and Cd^{2+} was extracted, and the concentration peak current curve was drawn. As shown in Fig. 12, the stripping peak current shows a good linear growth with the increase of Pb^{2+} concentration, the linear detection range of Pb^{2+} is 1–250 µg L^{-1}, and the linear regression equation is $I = 2.5769 \ln C - 0.1338$. As shown in Fig. 13, the linear detection range of Cd^{2+} is 1–250 µg L^{-1}, and the linear regression equation is $I = 1.3642 \ln C - 0.3683$. The lowest detection limits of Pb^{2+} and Cd^{2+} are 1 ng L^{-1}. The average relative standard deviations of Pb^{2+} and Cd^{2+} in the same sample are 3.1% and 5.8%, respectively. This method has high sensitivity, wide linear detection range, and good reproducibility.

3.5 Analysis of recovery experiment

Five concentration gradients of Pb^{2+} and Cd^{2+} (4, 8, 40, 100, and 200 µg L^{-1}) were selected within the linear detection range, and each concentration gradient was detected three times in parallel. The recovery rates are shown in Table 1. The recovery rate of each concentration gradient was in the range of 90.86–113.47%, indicating that the detection method had great precision and accuracy.

3.6 Analysis of interference experiment

Fig. 14 shows the influence of the stripping peaks of Pb^{2+} and Cd^{2+} by different heavy metal ions based on the interference experiment results when the concentrations of Pb^{2+} and Cd^{2+} are both 40 µg L^{-1}. Zn^{2+} and Cr^{3+} interfere minimally and have almost no effect on the stripping peak potential and stripping peak current of Pb^{2+}. Zn^{2+} causes the peak current of Pb^{2+} to decrease sharply and disappear. Cr^{3+} makes the peak potential of Cd^{2+} drift in a negative direction, affecting the peak current. The presence of Mn^{2+} decreases the stripping peak current of Pb^{2+} and Cd^{2+} to a certain extent. The interference of Cu^{2+} is maximum. Its stripping peak potential is very close to that of Pb^{2+}, considerably increasing the peak current of Pb^{2+} while causing the peak currents of Pb^{2+} and Cd^{2+} to disappear. The
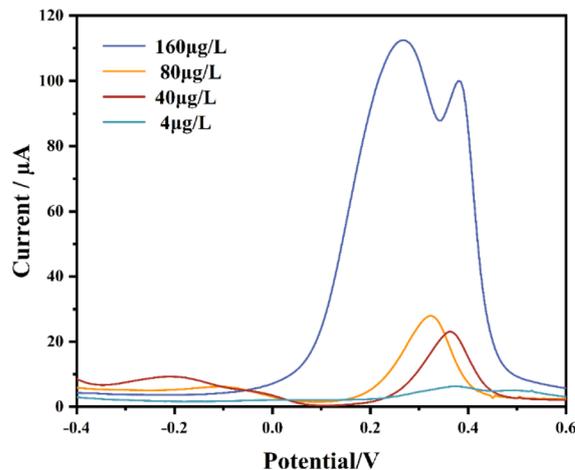
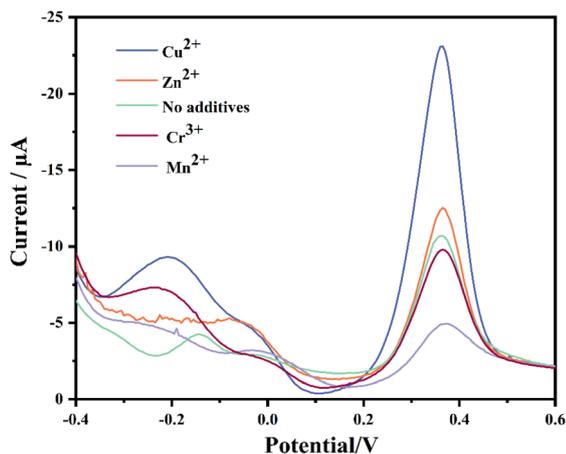Fig. 15 Stripping peaks of Pb^{2+} and Cd^{2+} under varying Cu^{2+} concentrations (*vs.* Ag/AgCl reference electrode).

reason may be related to the fact that the redox potential of Cu^{2+} is close to that of Pb^{2+}.[1,71] Moreover, some metal oxides that are not conducive to stripping analysis are generated, and they affect the electrochemical signal and the stripping peak potential.[62] Furthermore, adding Cu^{2+} causes hydrogen evolution, which is not conducive to heavy metal ion analysis. A corresponding masking agent can be added to the water to precipitate the interference ions, thereby eliminating the influence of interference ions on the detection and analysis.

The interference degree of Cu^{2+} was further investigated. All the other conditions remain unchanged. The influence of Cu^{2+} concentrations of 4, 40, 80, and 160 µg L^{-1} on the stripping peaks of Pb^{2+} and Cd^{2+} was investigated. The experiment data indicated that the increase of Cu^{2+} concentrations strengthens the interference degree to the peak currents of Pb^{2+} and Cd^{2+}, as shown in Fig. 15. Therefore, the selection of a suitable masking agent or complexing agent is expected to reduce or eliminate the interference of Cu^{2+}, but in such a way as to not affect the detection sensitivity of Pb^{2+} and Cd^{2+}.[72,73]

3.7 Real water sample analysis

The absorbance values of Pb^{2+} and Cd^{2+} standard solutions were measured by atomic absorption spectrophotometry, and the corresponding calibration curves are shown in Fig. S1.† The regression equations and correlation coefficients of Pb^{2+} and Cd^{2+} calibration curve (Table S3†).

The results of the electrochemical method applied in the real water sample are shown in Table 2. The comparison of Tables 2 and 1 indicated that the same electrochemical method was used to test real water samples and ABS, and the recoveries were slightly different in the two cases, which was mainly caused by the fact that the real water samples contained complex components, and different water samples had different components. Further qualitative determination of the components of the real water samples and optimization of experimental parameters are needed to improve the detection accuracy.

Fig. 14 Interference effects of coexisting heavy metal ions on the stripping peaks of Pb^{2+} and Cd^{2+} (*vs.* Ag/AgCl reference electrode).

Table 2 Comparative analysis of Pb^{2+} and Cd^{2+} detection in four real water samples: electrochemical method *vs.* atomic absorption spectrophotometry (AAS)

Sample	Metal ions	Electrochemical method			Atomic absorption spectrophotometry		
		Added ($\mu g\ L^{-1}$)	Found ($\mu g\ L^{-1}$)	Recovery (%)	Added ($\mu g\ L^{-1}$)	Found ($\mu g\ L^{-1}$)	Recovery (%)
Real water 1	Pb^{2+}	100	114.32	114.32	100	118.91	118.91
	Cd^{2+}		116.35	116.35		120.03	120.03
Real water 2	Pb^{2+}		110.14	110.14		106.56	106.56
	Cd^{2+}		109.46	109.46		90.45	90.45
Real water 3	Pb^{2+}		109.67	109.67		118.91	118.91
	Cd^{2+}		116.32	116.32		120.03	120.03
Real water 4	Pb^{2+}		85.36	85.36		106.56	106.56
	Cd^{2+}		119.32	119.32		116.34	116.34

As shown in Table 2, the comparison of the experimental results of the real water sample recovery by the electrochemical method and that by atomic absorption spectrophotometry indicated that the results of the two methods were basically the same. This electrochemical method has good application prospects in detecting heavy metal trace in the water environment, particularly acidic wastewater.[26]

4. Conclusion

This study established a high-performance three-electrode detection system through rational optimization of GNPs, integrating material engineering with analytical method innovation. Field emission scanning electron microscopy and electrochemical analyses demonstrated that precisely deposited gold nanoclusters with a $HAuCl_4$ concentration of 2 mmol L^{-1}, a deposition potential of 0.2 V, and a deposition time of 80 s increased the electrode's effective surface area by 7.2-fold, significantly enhancing electrochemical active sites and detection sensitivity. Coordinated optimization of electrolyte pH = 3.3 and square wave stripping parameters including a −4 V enrichment potential and 390 s enrichment time enabled ultra-trace quantification of Pb^{2+} and Cd^{2+}, achieving a broad linear range from 1 to 250 $\mu g\ L^{-1}$, an unprecedented detection limit of 1 ng L^{-1}, and satisfactory recovery rates spanning 90.86% to 113.47%. This method has been rigorously verified through analysis of real water samples and shows high consistency with atomic absorption spectrophotometry. The systematic parameter optimization—spanning morphology control, interfacial reaction kinetics modulation, and signal amplification strategy—establishes a universal framework for electrochemical detection system development, providing a rapid, sensitive, and field-applicable solution for heavy metal monitoring in aquatic environments, with significant potential to supplement conventional spectroscopic techniques.

In conclusion, this study has developed an ultrasensitive detection platform through the innovative integration of GNPs-Au architecture with advanced electrochemical sensing protocols. GNPs-Au demonstrates exceptional performance in simultaneous quantification of trace-level Pb^{2+} and Cd^{2+} contaminants in aqueous environments, achieving detection limits comparable to conventional spectroscopic methods while significantly improving detection limit. This advancement establishes a robust analytical framework for elucidating the speciation dynamics and transport mechanisms of heavy metal contaminants in environmental matrices. Furthermore, the proposed methodology provides critical technical support for deciphering complex synergistic effects in multi-contaminant systems, thereby paving the way for systematic investigations into compound pollution remediation mechanisms.

Data availability

The data that support the findings of this study are available from the corresponding author upon reasonable request.

Author contributions

Yuanping Li: conceptualization, funding acquisition, project administration, writing – review & editing, supervision. Shunyao Jia: investigation, writing – original draft, writing – review & editing. Yaoning Chen: funding acquisition, project administration, supervision. Yanting Wu: software, visualization, validation. Tianyun Zhou: investigation, visualization, validation. Nianping Chi: supervision, resources. Guo Wen He: resources, visualization. Wei Zhang: investigation, visualization. Wenqiang Luo: software. Hao Li: validation. Yumei Deng: investigation.

Conflicts of interest

The authors declare that they have no conflict of interest.

Acknowledgements

Safeguarding Drinking Water Quality in Hunan Villages and Towns Project (2019TP2079).

References

1 Y. Chen, M. Li, Y. Li, Y. Liu, Y. Chen, H. Li, L. Li, F. Xu, H. Jiang and L. Chen, *Bioresour. Technol.*, 2021, **321**, 124413, DOI: **10.1016/j.biortech.2020.124413**.

2 Y. Liu, Y. Chen, Y. Li, L. Chen, H. Jiang, H. Li, X. Luo, P. Tang, H. Yan, M. Zhao, Y. Yuan and S. Hou, *J. Hazard. Mater.*, 2022, **431**, 128584, DOI: **10.1016/j.jhazmat.2022.128584**.

3 Y. Chen, Y. Liu, Y. Li, L. Zhao, Y. Chen, H. Li, Y. Liu, L. Li, F. Xu and M. Li, *Environ. Sci. Pollut. Res.*, 2020, **27**, 38644–38653, DOI: **10.1007/s11356-020-09907-6**.

4 Y. Liu, Y. Chen, Y. Li, L. Chen, H. Jiang, M. Zhao, H. Li, C. Zhao, H. Kang and W. Zhou, *Sci. Total Environ.*, 2024, **920**, 170803, DOI: **10.1016/j.scitotenv.2024.170803**.

5 S. Bai, Z. Chang, Z. Ren, Y. Zhao and L. Pang, *RSC Adv.*, 2025, **15**, 11293–11300, DOI: **10.1039/D5RA00752F**.

6 Y. Chen, Y. Liu, Y. Li, Y. Wu, Y. Chen, G. Zeng, J. Zhang and H. Li, *Bioresour. Technol.*, 2017, **243**, 347–355, DOI: **10.1016/j.biortech.2017.06.100**.

7 J. Sendh and J. B. Baruah, *RSC Adv.*, 2024, **14**, 27153–27161, DOI: **10.1039/D4RA04655B**.

8 X. Zhang, J. Li, X. Li, Z. Chen, D. Ren and S. Zhang, *Environ. Geochem. Health*, 2025, **47**, 37, DOI: **10.1007/s10653-024-02352-1**.

9 K. Zhang, B. A. Kwadzokpui, S. Y.-S. S. Adade, H. Lin and Q. Chen, *Food Chem.*, 2024, **459**, 140305, DOI: **10.1016/j.foodchem.2024.140305**.

10 G. M. S. Alves, L. S. Rocha and H. Soares, *Talanta*, 2017, **175**, 53–68, DOI: **10.1016/j.talanta.2017.06.077**.

11 M. Soylak, H. E. H. Ahmed and M. Khan, *Sustainable Chem. Pharm.*, 2023, **32**, 101006, DOI: **10.1016/j.scp.2023.101006**.

12 D. Tibebe, M. Hussen, M. Mulugeta, D. yenealem, Z. Moges, M. Gedefaw and Y. Kassa, *BMC Chem.*, 2022, **16**, 87, DOI: **10.1186/s13065-022-00878-y**.

13 W. Chen, Y. Yang, K. Fu, D. Zhang and Z. Wang, *Front. Pharmacol.*, 2022, **13**, 891273, DOI: **10.3389/fphar.2022.891273**.

14 Z. Xu, J. Chen, Y. Liu, X. Wang and Q. Shi, *Chem. Eng. J.*, 2022, **441**, 135690, DOI: **10.1016/j.cej.2022.135690**.

15 Y. Wang, J. Qiao, S. Dong, S. Shao and D. Wang, *J. Hazard. Mater.*, 2023, **458**, 132003, DOI: **10.1016/j.jhazmat.2023.132003**.

16 W. Kim, W. Lee, H. Park, J. Park, W. Kim, B. Kang, E. Choi, C.-S. Kim, J.-O. Park, G. Lee, D. Bang and J. Park, *ACS Sustainable Chem. Eng.*, 2022, **10**, 3180–3190, DOI: **10.1021/acssuschemeng.1c07117**.

17 Q. Liu, C. Xu, S. Chu, S. Li, F. Wang, Y. Si, G. Mao, C. Wu and H. Wang, *J. Mater. Chem. B*, 2022, **10**, 10075–10082, DOI: **10.1039/d2tb01887j**.

18 Z. Cheng, J. Wei, L. Gu, L. Zou, T. Wang, L. Chen, Y. Li, Y. Yang and P. Li, *J. Hazard. Mater.*, 2022, **431**, 128606, DOI: **10.1016/j.jhazmat.2022.128606**.

19 K. Liu, M. Pan, Z. Zhang, L. Hong, X. Xie, J. Yang, S. Wang, Z. Wang, Y. Song and S. Wang, *Anal. Chim. Acta*, 2022, **1231**, 340392, DOI: **10.1016/j.aca.2022.340392**.

20 P. K. Mehta, H. Park, E.-T. Oh, H. J. Park and K.-H. Lee, *Sens. Actuators, B*, 2023, **385**, 133670, DOI: **10.1016/j.snb.2023.133670**.

21 I. A. Revesz, S. M. Hickey and M. J. Sweetman, *J. Mater. Chem. B*, 2022, **10**, 4346–4362, DOI: **10.1039/d2tb00408a**.

22 F. Qian, R. Jia, M. Cheng, A. Chaudhary, S. Melhi, S. D. Mekkey, N. Zhu, C. Wang, F. Razak, X. Xu, C. Yan, X. Bao, Q. Jiang, J. Wang and M. Hu, *Adv. Compos. Hybrid Mater.*, 2024, **7**, 75, DOI: **10.1007/s42114-024-00887-6**.

23 S. Tan, S. Li, C. Tang, X. Bai, X. Ran, Q. Qu, L. Li and L. Yang, *Talanta*, 2022, **246**, 123461, DOI: **10.1016/j.talanta.2022.123461**.

24 P. Ezati, A. Khan, J.-W. Rhim, J. T. Kim and R. Molaei, *Colloids Surf., B*, 2023, **221**, 113013, DOI: **10.1016/j.colsurfb.2022.113013**.

25 N. An, T. Chen, J. Zhang, G. Wang, M. Yan and S. Yang, *Small Mol.*, 2024, **8**, 2300910, DOI: **10.1002/smtd.202300910**.

26 P. S. Adarakatti, in *Agricultural Electrochemistry*, American Chemical Society, 2025, ch. 2, vol. 1496, pp. 17–46.

27 K. Fu, H. Sun, X. Chen, Y. Cao, L. Liu, J. Zhao, S. Li and W. Ma, *Food Chem.*, 2025, **465**, 142052, DOI: **10.1016/j.foodchem.2024.142052**.

28 S. Hu, S. Zhang, J. Qin, K. Cai, C. Peng, L. Luo, Y. Gu and Y. Mei, *Microchem. J.*, 2024, **205**, 111154, DOI: **10.1016/j.microc.2024.111154**.

29 G. A. Bodkhe, B. S. Hedau, M. A. Deshmukh, H. K. Patil, S. M. Shirsat, D. M. Phase, K. K. Pandey and M. D. Shirsat, *J. Mater. Sci.*, 2021, **56**, 474–487, DOI: **10.1007/s10853-020-05285-z**.

30 J. Zhao, Y. Long, C. He, H. Yang, S. Zhao, X. Luo, D. Huo and C. Hou, *ACS Sustainable Chem. Eng.*, 2023, **11**, 2160–2171, DOI: **10.1021/acssuschemeng.2c05240**.

31 R. S. Salama, E.-S. M. El-Sayed, S. M. El-Bahy and F. S. Awad, *Colloids Surf., A*, 2021, **626**, 127089, DOI: **10.1016/j.colsurfa.2021.127089**.

32 L. Yu, J. Zhang, J. Li, L. Sun, Q. Zhang, B. Yang, M. Huang and B. Xu, *Front. Chem.*, 2024, **12**, 1374898, DOI: **10.3389/fchem.2024.1374898**.

33 T. Zidarič, N. I. Hrastnik, E. Šest, J. Kovač, V. Jovanovski and S. B. Hočevar, *Sens. Actuators, B*, 2019, **291**, 354–361, DOI: **10.1016/j.snb.2019.04.106**.

34 C. Zhang, C. Li and X. Han, *J. Electroanal. Chem.*, 2023, **933**, 117291, DOI: **10.1016/j.jelechem.2023.117291**.

35 N. Lersanansit, K. Pungjunun, O. Chailapakul and N. Praphairaksit, *Talanta*, 2024, **276**, 126211, DOI: **10.1016/j.talanta.2024.126211**.

36 A. De Benedetto, A. Della Torre, M. Rachele Guascito, R. Di Corato, L. Chirivì, R. Rinaldi and A. Aloisi, *J. Electroanal. Chem.*, 2024, **964**, 118341, DOI: **10.1016/j.jelechem.2024.118341**.

37 K. Promsuwan, C. Sanguarnsak, K. Samoson, J. Saichanapan, A. Soleh, K. Saisahas, S. Wangchuk and W. Limbut, *Talanta*, 2024, **276**, 126179, DOI: **10.1016/j.talanta.2024.126179**.

38 C. E. Morgan, J. M. Bowling, J. Bartram and G. L. Kayser, *Int. J. Hyg. Environ. Health*, 2021, **236**, 113804, DOI: **10.1016/j.ijheh.2021.113804**.

39 X. Zhou, X. Wang and L. Shang, *Chin. Chem. Lett.*, 2023, **34**, 108093, DOI: **10.1016/j.cclet.2022.108093**.

40 R. Sanchis-Gual, M. Coronado-Puchau, T. Mallah and E. Coronado, *Coord. Chem. Rev.*, 2023, **480**, 215025, DOI: **10.1016/j.ccr.2023.215025**.

41 T. Xiao, J. Huang, D. Wang, T. Meng and X. Yang, *Talanta*, 2020, **206**, 120210, DOI: **10.1016/j.talanta.2019.120210**.

42 N. Mohamad Nor, S. N. Nasrul, N. D. Zakaria and K. Abdul Razak, *ACS Omega*, 2023, **8**, 16587–16599, DOI: **10.1021/acsomega.2c07085**.

43 G. Zhao, H. Wang, G. Liu, Z. Wang and J. Cheng, *Ionics*, 2017, **23**, 767–777, DOI: **10.1007/s11581-016-1843-6**.

44 L. Zhu, L. Xu, B. Huang, N. Jia, L. Tan and S. Yao, *Electrochim. Acta*, 2014, **115**, 471–477, DOI: **10.1016/j.electacta.2013.10.209**.

45 M. Quansah, L. Fetter, A. Fineran, H. V. Colling, K. Silver, T. J. Rowland and A. J. Bonham, *Biosensors*, 2023, **13**, 675, DOI: **10.3390/bios13070675**.

46 D. Probst, I. Lee and K. Sode, *Electrochim. Acta*, 2022, **426**, 140798, DOI: **10.1016/j.electacta.2022.140798**.

47 J. Lee, K.-Y. Kim, Y. Kwon and D.-Y. Khang, *Adv. Funct. Mater.*, 2024, **34**, 2309386, DOI: **10.1002/adfm.202309386**.

48 A. Nsabimana, S. A. Kitte, T. H. Fereja, M. I. Halawa, W. Zhang and G. Xu, *Curr. Opin. Electrochem.*, 2019, **17**, 65–71, DOI: **10.1016/j.coelec.2019.04.012**.

49 C. Wang, F. Ren, C. Zhai, K. Zhang, B. Yang, D. Bin, H. Wang, P. Yang and Y. Du, *RSC Adv.*, 2014, **4**, 57600–57607, DOI: **10.1039/C4RA08949A**.

50 G. Korotcenkov, L. B. Gulina, B. Cho, V. Brinzari and V. P. Tolstoy, *Pure Appl. Chem.*, 2014, **86**, 801–817, DOI: **10.1515/pac-2013-1102**.

51 M. H. M. Zaki, Y. Mohd and L. Y. Chin, *Int. J. Electrochem. Sci.*, 2020, **15**, 11401–11415, DOI: **10.20964/2020.11.41**.

52 S. R. Nambiar, P. K. Aneesh and T. P. Rao, *J. Electroanal. Chem.*, 2014, **722–723**, 60–67, DOI: **10.1016/j.jelechem.2014.03.011**.

53 H. Yang, X. Li, Q. Wu, H. Su, C. Ma, X. Wang, C. Xie and D. Zeng, *Sens. Actuators, B*, 2023, **376**, 133033, DOI: **10.1016/j.snb.2022.133033**.

54 X. Jiang, Y. Zhen, Y. Feng, Z. Yang and Z. Qin, *J. Alloys Compd.*, 2023, **938**, 168520, DOI: **10.1016/j.jallcom.2022.168520**.

55 R. B. Manami, M. B. Megalamani, R. G. Kalkhambkar, S. T. Nandibewoor, P. S. Adarakatti, M. S. Refat, A. M. Alsuhaibani and M. Arshad, *Ionics*, 2025, **31**, 3757–3773, DOI: **10.1007/s11581-025-06155-x**.

56 Y. Li, H. Huang, R. Cui, D. Wang, Z. Yin, D. Wang, L. Zheng, J. Zhang, Y. Zhao, H. Yuan, J. Dong, X. Guo and B. Sun, *Sens. Actuators, B*, 2021, **332**, 129519, DOI: **10.1016/j.snb.2021.129519**.

57 P. Shivappa Adarakatti, C. W. Foster, C. E. Banks, A. K. N. S and P. Malingappa, *Sens. Actuators, A*, 2017, **267**, 517–525, DOI: **10.1016/j.sna.2017.10.059**.

58 R. Espinoza, D. V. Cahua, K. Magro and S. C. Nguyen, *J. Phys. Chem. Lett.*, 2024, **15**, 12243–12247, DOI: **10.1021/acs.jpclett.4c02998**.

59 P. Lertsathitphong, A. P. O'Mullane and B. Lertanantawong, *Colloids Surf., A*, 2020, **592**, 124580, DOI: **10.1016/j.colsurfa.2020.124580**.

60 J. Li, Y. Wang, Y. Jiao, R. Jia and Z. Chen, *Microchim. Acta*, 2017, **184**, 3817–3823, DOI: **10.1007/s00604-017-2409-7**.

61 I. Leka Kottaiveedu Sivakumar, L. Bouffier, N. Sojic and S. Senthil, *Kumar*, 2025, **64**, e202421185, DOI: **10.1002/anie.202421185**.

62 P. S. Adarakatti, A. Siddaramanna and P. Malingappa, *Anal. Methods*, 2019, **11**, 813–820, DOI: **10.1039/C8AY02648C**.

63 D. Ratih Purwaningsih, U. Pengsomjit, M. Aly Saad Aly, I. A. Darwish, C. Karuwan and C. Kraiya, *Microchem. J.*, 2024, **206**, 111449, DOI: **10.1016/j.microc.2024.111449**.

64 Y. Li, R. Cui, H. Huang, J. Dong, B. Liu, D. Zhao, J. Wang, D. Wang, H. Yuan, X. Guo and B. Sun, *Anal. Chim. Acta*, 2020, **1125**, 76–85, DOI: **10.1016/j.aca.2020.05.036**.

65 H. Jiang, Z. Yi, Y. Chen, Y. Li, L. Chen, J. Wang, Y. Nie, M. Luo, Q. Wang and W. Zhang, *Sci. Total Environ.*, 2025, **959**, 178236, DOI: **10.1016/j.scitotenv.2024.178236**.

66 H. Jiang, Y. Chen, Y. Li, L. Chen, J. Wang, H. Kang, Y. Chen, C. Zhao, Y. Nie and S. Jia, *J. Environ. Chem. Eng.*, 2024, **12**, 113775, DOI: **10.1016/j.jece.2024.113775**.

67 P. S. Adarakatti and P. Malingappa, *J. Solid State Electrochem.*, 2016, **20**, 3349–3358, DOI: **10.1007/s10008-016-3306-4**.

68 T. Wu, Y. Zhu, L. Song, Y. Chen, Y. Huang, J. Tang, X. Ma, H. Wang, J. Zhang, D. Lin and G. Chen, *Anal. Methods*, 2022, **14**, 859–868, DOI: **10.1039/D1AY02051J**.

69 A. Seifi, A. Afkhami and T. Madrakian, *J. Appl. Electrochem.*, 2022, **52**, 1513–1523, DOI: **10.1007/s10800-022-01728-4**.

70 R. B. Manami, M. B. Megalamani, Y. N. Patil, R. G. Kalkhambkar, S. T. Nandibewoor, P. S. Adarakatti, M. S. Refat, M. Arshad and A. M. Alsuhaibani, *Top. Catal.*, 2025, DOI: **10.1007/s11244-025-02087-y**.

71 Y. Chen, Y. Yuan, Y. Li, L. Chen, H. Jiang, J. Wang, H. Li, Y. Chen, Q. Wang and M. Luo, *Sci. Total Environ.*, 2024, **924**, 171600, DOI: **10.1016/j.scitotenv.2024.171600**.

72 M. Chen, H. Liu, J. Pan, S. He, Y. Hong, S. Wang, Y. Zhou, D. Chen and M. Su, *Ecotoxicol. Environ. Saf.*, 2024, **282**, 116702, DOI: **10.1016/j.ecoenv.2024.116702**.

73 B. Deng, X. Xu, Y. Xiao, P. Zhu and Y. Wang, *Anal. Chim. Acta*, 2015, **853**, 179–186, DOI: **10.1016/j.aca.2014.10.034**.